Influence of CFRC insert on spark plasma sintering process investigated by experiment and finite element modeling

Alexander M. Laptev [1,*], Jürgen Hennicke [2], Robert Ihl [2]

[1] Łukasiewisz Research Network - Metal Forming Institute, Jana Pawla II Str. 14, 61-139 Poznań, Poland, laptev@gmx.net (A.M.L.)

[2] FCT Systeme GmbH, Rauenstein Gewerbepark 16, 96528, Frankenblick, Germany, j.hennicke@fct-systeme.de (J.H.); r.ihl@ fct-systeme.de (R.I.)

* Correspondence: laptev@gmx.net

Received: 29 May 2021; Accepted: 13 July 2021; Published: date

Abstract. Spark Plasma Sintering (SPS) is a technology used for a fast consolidation of metallic, ceramic, and composite powders. The upscaling of this technology requires a reduction in energy consumption and homogenization of temperature in compacts. The application of Carbon Fiber-Reinforced Carbon (CFRC) insulation plates between the sintering setup and the electrodes is frequently considered as a measure to attain these goals. However, the efficiency of such a practice remains largely unexplored so far. In the present paper, the impact of CFRC plates on required power, total sintering energy, and temperature distribution was investigated by experiments and by a Finite Element Method (FEM). The study was performed at a temperature of 1000°C with a graphite dummy mimicking an SPS setup. A rather moderate influence of CFRC plates on power and energy demand was found. Furthermore, the cooling stage becomes considerably longer. However, the application of CFRC plates leads to a significant reduction in the axial temperature gradient. The comparative analysis of experimental and modeling results showed the good capability of the FEM model for the prediction of temperature distribution and required electric current. However, the discrepancy between measured and calculated voltage and power was relatively high. This feature must be further investigated considering the pulsing character of the applied electric field.

Keywords: spark plasma sintering; carbon fiber-reinforced carbon; finite element modeling; energy consumption; temperature distribution

1. Introduction

Spark plasma sintering (SPS) also known as field assisted sintering technique (FAST) is an advanced technology for fast sintering of metallic, ceramic and composite powders [1,2]. The short sintering time at FAST/SPS is achieved by rapid resistance (Joule) heating, application of mechanical pressure and due to activation of some intrinsic sintering mechanisms by electric field and direct current (DC) or pulsed direct current (PDC) [1-6]. Nowadays, FAST/SPS process is in transition from laboratory scale to industrial application [7,8]. This development leads to new challenges for researchers, designers and processing engineers which must be addressed. In particular, the enhanced productivity of FAST/SPS units, sintering of large sized parts with complex shape, reliable insurance of required quality must be achieved. Finally, the FAST/SPS technique should be economically competitive with other pressure-assisted sintering technologies such as conventional hot pressing, hot isostatic pressing or powder forging. From this standpoint, two matters become a special importance. The first point is the energy efficiency. This is a prerequisite for economic benefit but also an important issue of technical efficiency. Reduction in required power enables the use of cheaper power source with lower capacity, increase in productivity (with higher heating rates and shorter sintering cycle), sintering of larger parts, better condition for exploitation of other components in a FAST/SPS device e.g. transformer and cooling system. Early, Laptev et al. have shown that power and energy consumption during FAST/SPS can be drastically diminished by proper insulation of the sintering tool [9]. Besides thermal insulation of external die surfaces for reduction of radiation losses, an insulation of FAST/SPS tool from water-cooled electrodes was considered. In a small FAST/SPS machine (HP D5, FCT Systeme, Rauenstein, Germany) this was

realized by application of conical spacers made from carbon fiber-reinforced carbon composite (CFRC) with low thermal conductivity but with acceptable electrical conductance [9]. However, in regular practice a CFRC plate placed between conical protection plate and water-cooled electrode is rather used. The influence of such an insulating plate on total energy balance is unexplored so far. The second point is the understanding of the temperature distribution within the FAST/SPS setup and especially in the sintered part. This is a matter of importance for a meaningful temperature control and for the evaluation of homogeneity in density and other properties within the sintered part. This topic was partly investigated for FAST/SPS setup with CFRC conical protection plates [9]. The positive influence of CFRC insulation on temperature distribution was noticed. The diminishing in temperature gradients was more evidenced for parts of large size. This result was obtained mainly theoretically by finite element method (FEM). Therefore, an experimental validation of this conclusion is desirable. In particular, the effect of more relevant to practice CFRC insulating plates has to be studied.

In the present paper the influence of such a plate was studied using two setups. In the first setup the CFRC plates were not used. In the second setup the FAST/SPS tool was insulated from water-cooled electrodes by CFRC plates. Total energy, power, current, voltage and temperature of electrodes were recorded during FAST/SPS cycles. Temperature and voltage distributions within the setup were experimentally studied and compared with the results of a FEM analysis. The effect of CFRC insulating plates on energy balance and temperature distribution was evidenced. The accuracy of a newly updated finite element model for the prediction of thermal, electrical and energetic parameters of FAST/SPS was evaluated and discussed.

2. Experimental

The sketches of used setups are presented in Figure 1. Besides, a part of the Copper alloy electrodes is shown. The first setup (Figure 1a) consists of a one-piece graphite dummy and two graphite spacers. In the second setup (Figure 1b) two CFRC plates with a thickness of 10 mm are additionally placed between spacers and electrodes. The dummy and the both spacers were manufactured from isostatically pressed R 7710 graphite (SGL Carbon GmbH, Meitingen, Germany). The Sigrabond® Premium CFRC composite from the same supplier was used for the additional plates. The graphite dummy mimicked a SPS setup with the 10 mm hole for temperature measurement by an axial pyrometer. The use of a dummy instead of a real SPS setup was caused by two main reasons. First, a setup with this dummy does not have vertical contacts such as punch/die in a regular SPS setup. Their resistance to current and heat flow is high and usually not well defined. Therefore, the presence of vertical contacts can influence the experimental and modeling results in an unpredictable way. Therefore, to verify any hypothesis or theory, the application of dummy may be preferable. Second, in contrast to a regular SPS setup, the dummy enables convenient temperature measurement in any point including its geometrical center (i.e. at location T_1). In the used dummy, the temperature was recorded at three locations marked in Figure 1 as T_1 (0, 6), T_2 (9, 36) and T_3 (9, 53). The numbers in brackets denote the R and Z coordinates of a metering point. In addition, the temperature was measured in the spacer at location T_4 (9, 105) and in the water-cooled electrode at location T_5 (12.5, 135 or 145). Furthermore, the used dummy provided the measurement of voltage drop between all these points and symmetrically located ones U_1, U_2, U_3, U_4 and U_5.

The experiments were performed in a HP D25 facility (FCT Systeme, Rauenstein, Germany) under a medium vacuum of 0.4 hPa. A pulsed direct current (PDC) with 25 ms pulse and 5 ms pause pattern was used for heating. The thermocouple in location T_1 sent an input signal to the PID controller adjusting the supplied power and generating a prescribed temperature cycle. The dummy was heated-up at the rate of 100°C/min till a temperature of 1000°C in location T_1. The next segment included dwell at 1000°C for 5 min. In one cycle, the holding time was reduced to 1 min. The last segment was natural cooling to room temperature. A load of 44 kN was applied during the entire heating cycle.

The current and voltage tapped after the transformer were recorded during the entire FAST/SPS cycles. Thereby, the pulsed current and voltage were averaged by the root mean square method, i.e. as I_{RMS} and U_{RMS}. The consumed power was defined as a product of these quantities i.e. $\dot{Q}_{RMS} = I_{RMS} \cdot U_{RMS}$. Thus, the possible phase difference between current and voltage was not considered. All data were recorded every second. The energy increment was determined as a product of power and time increment. The total energy was calculated as a sum of energy increments. The temperatures at the locations

described above were measured by *K*-type thermocouples. Thermocouples were also used as the leads for voltage measurement. The performed experiments are summarized in Table 1 for the regular setup, and in Table 2 for the setup with CFRC plates.

Table 1. Measurements with regular setup.

Position	**1**	**2**	**3**	**4**	**5**
Temperature	**x**	**x**	**x**	**x**	**x**
Voltage	**-**	**x**	**-**	**x**	**-**

Table 2. Measurements with CFRC plates.

Position	**1**	**2**	**3**	**4**	**5**
Temperature	**x**	**x**	**x**	**x**	**x**
Voltage	**-**	**-**	**-**	**x**	**x**

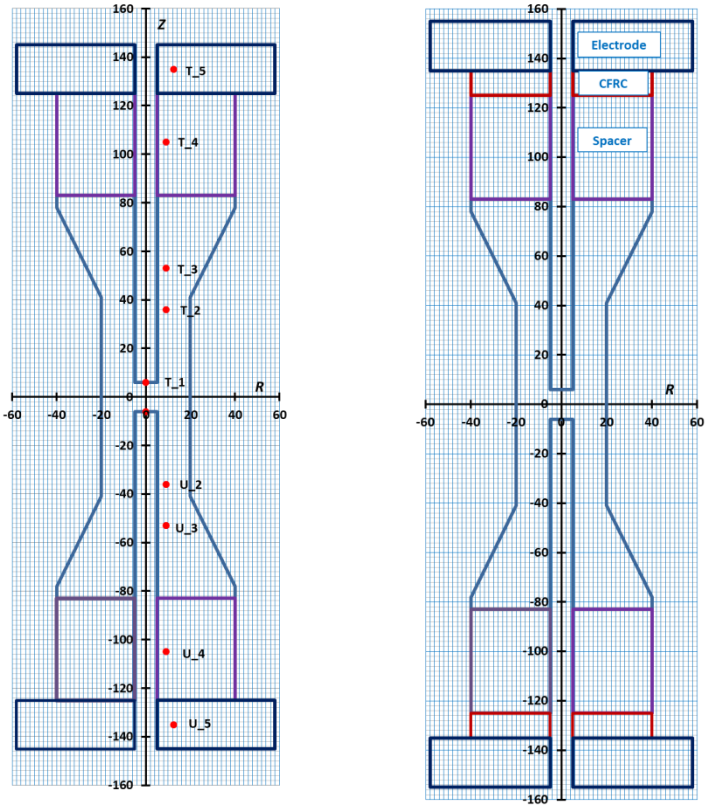

Figure 1. Sketch of used setups: **(a)** regular setup and **(b)** setup with CFRC plates. The locations of temperature and voltage test points are indicated by red marker.

3. FEM modeling

3.1. Basic equations

The total power balance during FAST/SPS is described by the following equation.

$$\dot{Q}_e = \dot{Q}_h + \dot{Q}_l \,. \tag{1}$$

Here $\dot{Q}_e$ = power supplied to the FAST/SPS setup by an external power source; $\dot{Q}_h$= power required for heating; $\dot{Q}_l$ = thermal losses. For simplification of modeling, the real PDC current was replaced by an equivalent DC. Thus, the possible electromagnetic effects of current pulsing were not considered. The

same procedure was applied to the electric field and voltage. The electric power was determined by the Joule's law (2) taking into account the Ohm's law (3).

$$\dot{Q}_e = \int_V \dot{q}_e \cdot dV = \int_V \{i\} \cdot \{E\}^T \cdot dV = \int_V [\sigma] \cdot \{E\} \cdot \{E\}^T \cdot dV \quad (2)$$

$$\{i\} = [\sigma] \cdot \{E\}. \quad (3)$$

Here $\dot{q}_e$ = specific Joule's power; $\{i\}$ = current density vector; $\{E\}$ = electric field vector; $[\sigma]$ = diagonal matrix of electrical conductivity, V = volume of FAST/SPS setup. The entries of $[\sigma]$ matrix are functions of temperature. For an isotropic material all entries of this matrix are equal to each other. The heating power was calculated as

$$\dot{Q}_h = \int_V c_p \cdot \rho \cdot \dot{T} \cdot dV \quad (4)$$

Here c_p = specific heat capacity; ρ = density. Both properties vary with temperature. Thermal power losses are a sum of three components: the radiation loss ($\dot{Q}_r$), the heat loss due to cooling of electrodes ($\dot{Q}_c$) and the heat loss owing to the electrical contact resistances ($\dot{Q}_{cr}$), i.e.

$$\dot{Q}_l = \dot{Q}_r + \dot{Q}_c + \dot{Q}_{cr.} \quad (5)$$

The radiation heat loss was modeled by the Stefan-Boltzmann law

$$\dot{Q}_r = \int_{S_e} \sigma_S \cdot \varepsilon \cdot (T_e^4 - T_a^4) \cdot dS_e. \quad (6)$$

Here σ_S = Stefan-Boltzmann constant; ε = emissivity; T_e = temperature of external surface of a FAST/SPS setup; T_a = ambient temperature and S_e = area of radiating surface. The heat loss due to cooling of electrodes was considered as the conductive heat transfer from electrode to cooling water. This process was modeled by the Newton's law of cooling.

$$\dot{Q}_c = \int_{S_c} h \cdot (T_c - T_w) \cdot dS_c. \quad (7)$$

Here h = heat transfer coefficient; T_c = temperature of cooled surface; T_w = temperature of cooling water and S_c = area of cooled surface. The heat resulting from electrical contact resistance was calculated by the formula

$$\dot{Q_{cr}} = \int_{S_{ca}} \sigma_c \cdot [U_c]^2 \cdot dS_{ca}. \quad (8)$$

Here σ_c = electric conductance per unit area; $[U_c]$ = voltage (i.e. electric potential) drop over the contact surface and S_{ca} = contact area. The electric field in the setup was modeled by the Faraday's law.

$$\{E\} = -\nabla \cdot \{U\}^T. \quad (9)$$

Here $\{U\}$ = electrical potential vector. In a similar manner, the thermal field was simulated by the Fourier's law.

$$\{\dot{q}\} = -[\lambda] \cdot \nabla T. \quad (10)$$

Here $\{\dot{q}\}$ = heat flux density vector; $[\lambda]$ = thermal conductivity matrix; ∇T = temperature gradient. The thermal flux through unit contact surfaces was calculated by the formula

$$\dot{q_{ct}} = \int_{S_{ca}} \lambda_c \cdot [T_c] \cdot dS_{ca}. \quad (11)$$

Here λ_c = thermal conductance of unit area; $[T_c]$ = temperature drop over the contact surface and S_{ca} = contact area. More detail about the used mathematical model can be found in our previous papers [9,10].

3.2. Properties

3.2.1. Bulk properties

The density, electrical resistivity and thermal conductivity for graphite R 7710 were taken from manufacturer (SGL Carbon GmbH, Germany). The specific heat capacity for graphite was borrowed from the paper by McDonalds [11]. These data are presented in graphical form in the previous paper by Laptev [9]. The properties of Copper alloy were taken from supplier. The density and specific heat capacity and thermal conductivity in plane and for CFRC grade 1501G were taken from SGL Carbon brochure [12]. The CFRC is a strongly anisotropic material. Therefore, the thermal conductivity and electrical resistivity must be considered in the carbon fabric plane and in the perpendicular direction. The data for thermal conductivity in both directions are available in the SGL Carbon brochure [12]. However, the resistivity of CFRC is provided only in the plain of carbon fabric. Therefore, a special experiment was performed for determination of CFRC resistivity in the perpendicular direction.

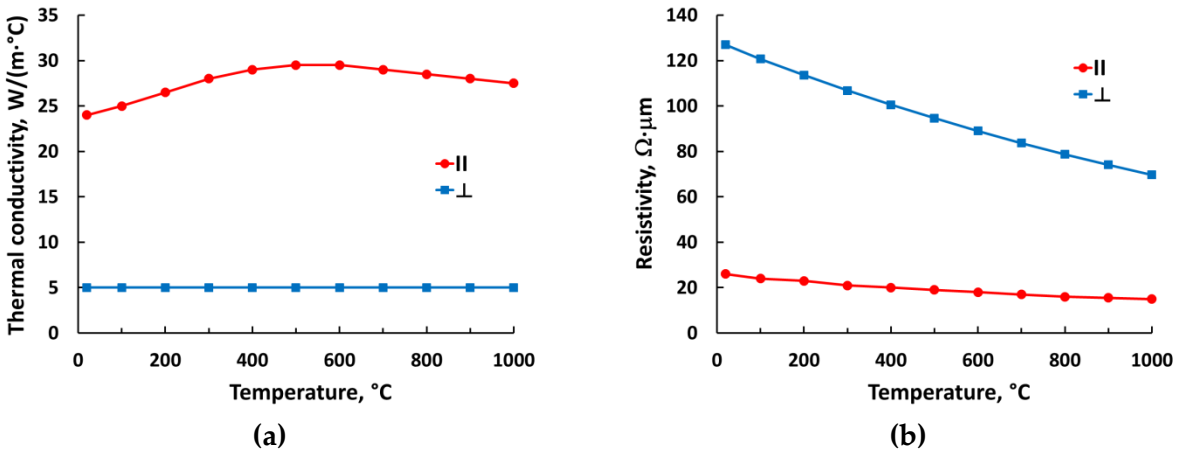

Figure 2. Thermal conductivity **(a)** and electrical resistivity **(b)** of CFRC plate: in plane of carbon fabric (**II**) and in perpendicular direction (⊥).

3.2.2. Contact properties

The elements of both discussed setups have merely horizontally placed contact surfaces. The contacts are pressurized by the hydraulic cylinder of the SPS device. The electrical and thermal conductivity of horizontal contacts are high, and even may be not considered in the FEM modeling [13]. However, electrical and thermal contact properties must be described in the FEM model to enable

appropriate numerical analysis. In our paper the specific electric conductivity of horizontal contacts σ_c was described with the empirical formula (12) proposed by Wei et al. [14].

$$\sigma_c = \frac{10}{(-0.24 \cdot lnT + 1.94) \cdot (27.61 \cdot p^{-1.09})} \frac{S}{mm^2}, \quad (12)$$

Here T = temperature (°C) and p = contact pressure (MPa). In our model all contact surfaces have the shape of a disc with an external diameter of 80 mm and with a central hole of 10 mm in diameter. With an applied load of 45 kN during entire SPS cycle the contact pressure was p = 9 MPa. The specific thermal conductivity of contacts at various temperatures λ_c was taken from the paper by Vanmeensel et al. [15].

3.3. Modeling procedure

The ANSYS® Mechanical APDL 15.0 software (ANSYS Inc., Canonsburg, USA) was used for finite element modeling. The model was implemented as an APDL input file.

3.3.1. Geometry and meshing

Due to rotational symmetry only a half of the entire configuration was considered. The quadrilateral-shaped, axisymmetric PLANE 223 element with thermal-electrical capability and with a size of around 2 mm was used. The combination of free and mapped (where possible) meshing was applied. Contact interaction was modeled by TARGE169 and CONTA171 elements.

3.3.2. Initial, boundary conditions and load

An initial temperature of 25°C was taken for entire setup. A heat transfer coefficient of h = 2870 W/(m^2·°C) was applied on internal surfaces of water-cooled electrode. With this value the best conformity with measured temperature of electrode (T_5) has been achieved. A constant temperature of cooling water of Tw = 25.5°C was used. This value was measured at the outlet of the HP D25 cooling system. According to recommendations published by Zavaliangos et al. an emissivity coefficient of 0.8 was taken for graphite (the dummy and the spacers) [16]. An emissivity of 0.2 was applied on external surfaces of Copper alloy electrodes. An emissivity coefficient of 0.945 within all internal holes of setup was assumed. The electric potential on the bottom of the lower electrode was set to zero. A time-varying voltage was applied on the top of the upper electrode. This voltage was tuned by the virtual PID controller to generate the predetermined time-temperature profile. The voltage on the top was set to zero during cooling.

3.3.3. Virtual PID controller

The standard PID algorithm was applied. Temperature in location T_1 (Figure 1) was considered as the process variable. Voltage on the top $u(t)$ was taken as the control variable. Accordingly, the control function can be expressed by equation (12).

$$u(t) = K_p \cdot \Delta T(t) + K_i \cdot \int_0^t \Delta T(t) \cdot dt + K_d \cdot \frac{d}{dt} \Delta T(t). \quad (12)$$

Here K_p = proportional gain; K_i = integral gain; K_d = derivative gain; t = instantaneous time; $\Delta T(t) = T_s(t) - T_c(t)$ = error; $T_s(t)$ = set temperature and $T_c(t)$ = calculated temperature. The control function was rearranged to finite difference form.

$$u(t) = K_p \cdot \Delta T(t) + K_i \cdot \sum_0^\tau \Delta T(t) \cdot \Delta t + K_d \cdot \frac{\Delta(\Delta T(t))}{\Delta t}. \quad (13)$$

Here Δt = time step; $\tau = n \cdot \Delta t$ = total time; n = time steps number. The control function (13) was integrated into APDL code. The tuning of the PID controller was done manually: First, the proportional

gain was adjusted. Then integral gain and finally derivative gain were tuned. With a time step of 1 s a good accuracy in generation of predefined time-temperature profile was achieved. Earlier, Muñoz and Anselmi-Tamburini developed similar virtual PID controller [17]. A main distinguishing feature of this controller was the use of current as the control variable.

4. Results

4.1. Influence of CFRC plates on general parameters

The influence of CFRC plates on the temperature development at T_1 (center of dummy) and T_5 (upper electrode) locations is shown in Figure 3. The first distinguishing feature is the slower cooling for the setup with CFRC plates. The second peculiarity is the lower temperature of the water-cooled electrode. Both these issues evidence the reduced heat flow from setup towards electrodes. Thus, a reduction of temperature gradients in axial direction can be expected. The lower temperature of electrodes is beneficial for the entire cooling system. In particular, less energy for cooling is needed. However, for the setup with CFRC plates a longer cooling time is required.

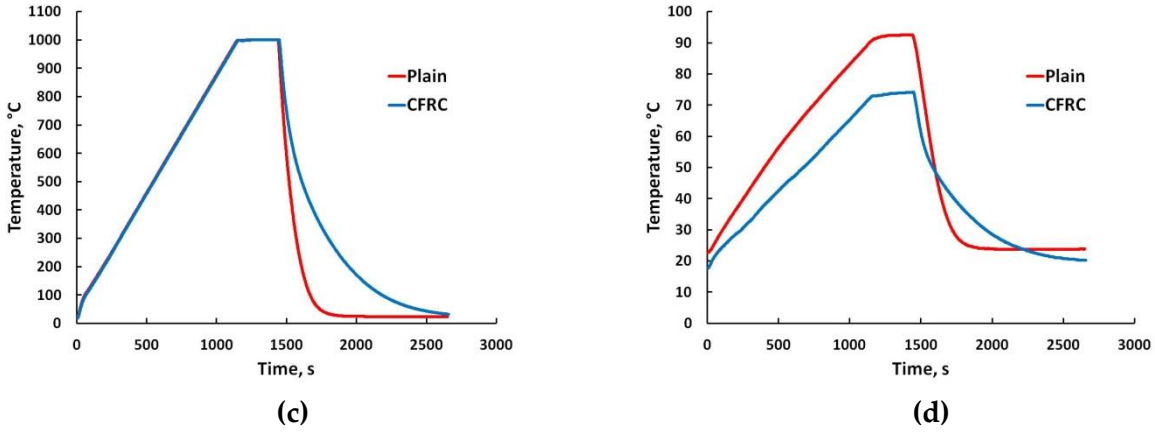

Figure 3. Temperature evolution recorded at **(a)** T_1 and **(b)** T_5 locations.

The impact of CFRC plates on the electrical quantities, power and energy is shown in Figure 4. The application of CFRC plates hardly influences the voltage measured after transformer. An additional resistance in the circuit, originated from CFRC plates, explains a small increase in voltage. However, the electric current is notably less if CFRC plates are used. As a result, the power needed for heating and following holding is lower with CFRC plates. Accordingly, the overall energy consumed during FAST/SPS cycle is reduced when CFRC plates are used. The reduction in energy is rather moderate. However, this effect can be more noticeable during sintering at higher temperatures.

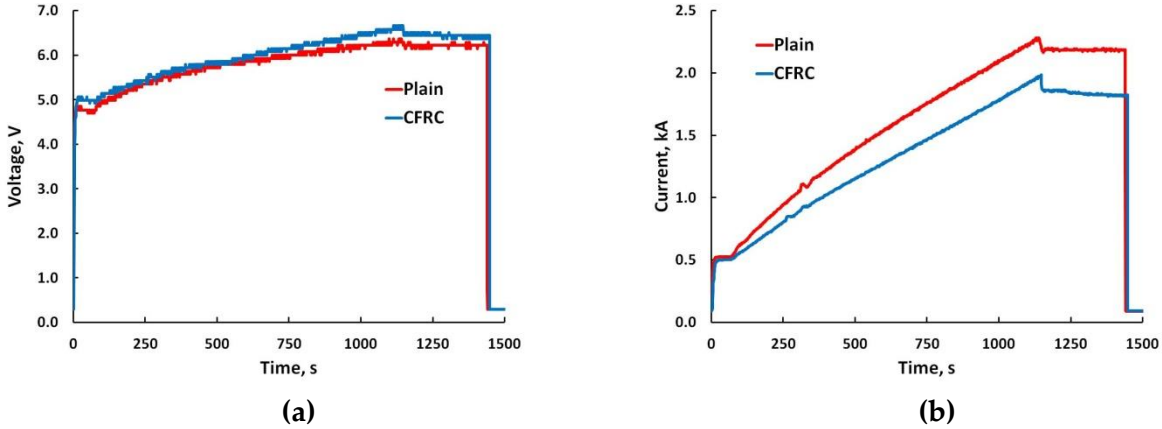

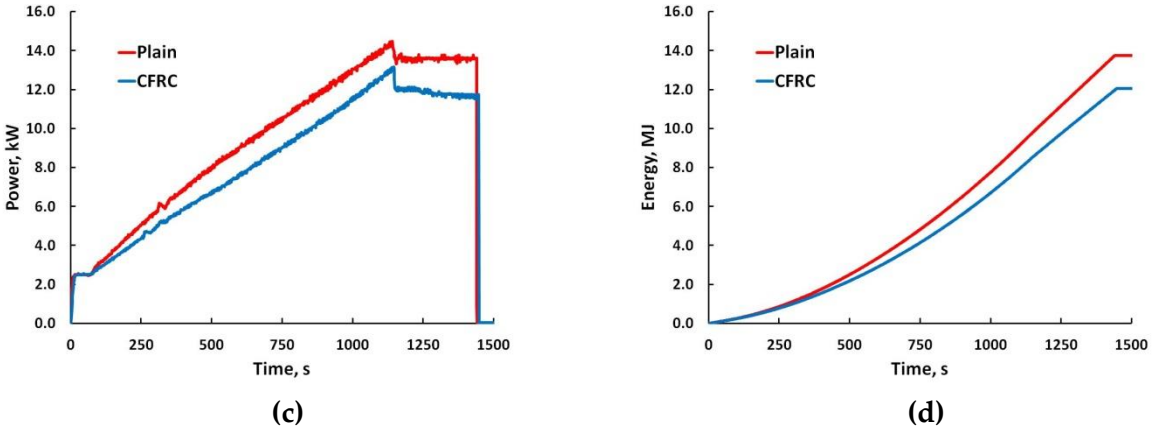

Figure 4. Influence of CFRC insert on: **(a)** voltage, **(b)** current, **(c)** total heater power and **(d)** consumed energy.

4.2. Influence of CFRC insert on local parameters

Figure 5 shows the temperature distribution in the whole setup and in the dummy after 200 s holding. The temperature contours were obtained by FEM modeling as discussed in Section 3. The contours evidence the large temperature gradient in axial direction. At first sight, the temperature distribution in both setups appears similar. However, more detailed observation shows a reduced temperature gradient in the setup with CFRC plates. This feature becomes more readable in Figure 6, where the temperatures in the reference points are considered. The temperature development, recorded by thermocouples in regular setup, is presented in Figure 6a. The temperature, measured in the setup with CFRC plates, is shown in Figure 6b. In both diagrams, the results of FEM modeling are also included. The measured and calculated temperatures are in good agreement. This means, that the set of properties, used for modeling, is reasonable, and the boundary conditions are meaningful. In addition, the accuracy in tuning of temperature profile by the virtual PID controller is evidenced. The temperature, developed in the electrode, is shown in Figure 6c for the regular setup and in Figure 6d for the setup with CFRC plates. The good agreement of experimental and modeled results during heating and holding stages for the regular setup is visible. At the same time, a certain discrepancy between measured and calculated data for the setup with CFRC is observed. This can be caused by any inaccuracies of the CFRC thermal properties applied for FEM modeling. However, the difference of experimental and modeling results is only 8°C or less.

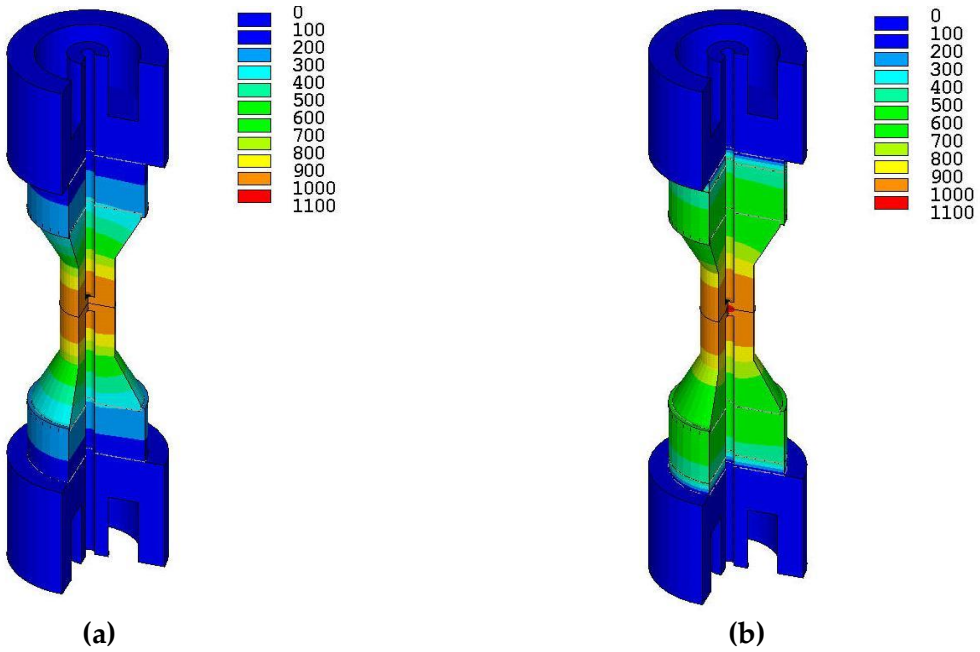

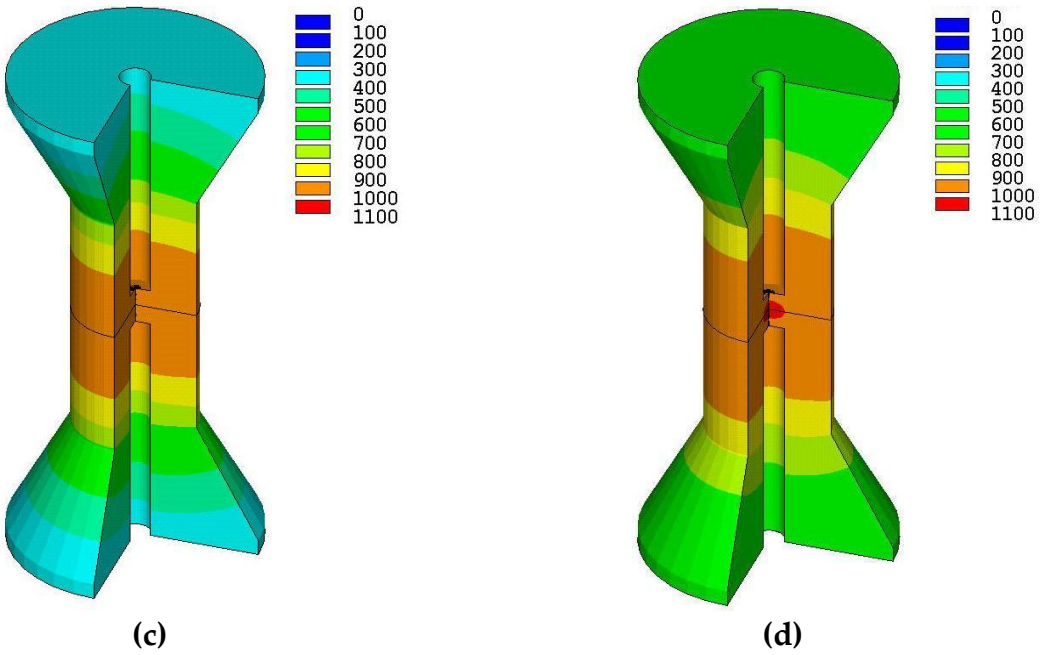

Figure 5. Modeled temperature distribution at 1200 s (holding stage): **(a)**-**(b)** in entire setup and **(c)**-**(d)** in dummy. Left –regular setup, right – setup with CFRC insert.

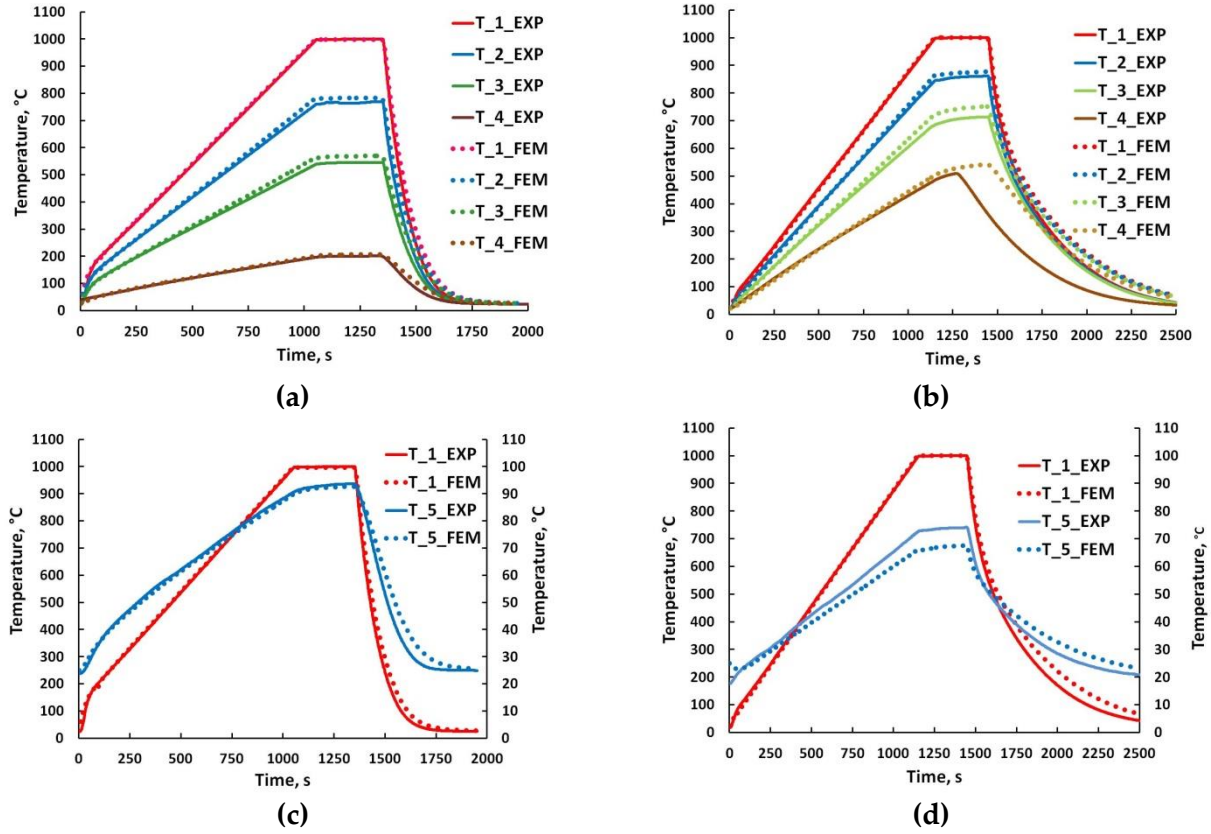

Figure 6. Temperature development as recorded by thermocouples (solid lines) and modeled by FEM (dotted lines): **(a)**, **(c)** in regular setup; **(b)**, **(d)** in setup with CFRC insert. T1-T3 – temperature in dummy; T4 – temperature in graphite spacer; T5 – temperature in electrode.

The application of CFRC plates leads to an increase of the system resistance, and as a result to an increase of the related voltage drop. This is clearly visible from the comparison of the FEM modeled voltage contours in both setups presented in Figure 7. The current, required for heating, grows with increase in temperature (Figure 8a and Figure 8b). This is mainly a result of increase in graphite specific

thermal capacity at rising temperature [15]. As it was already mentioned above, the current is lower with the application of CFRC plates. The comparison of measured and modeled current profiles in Figure 8a and Figure 8b shows a good agreement in both cases. Thus, the used approach and FEM code are suitable for electric current modeling. The situation with voltage modeling is different. The voltage in the reference points grows during heating similar to the current (Figure 8c and Figure 8d). However, the discrepancy between measured and modeled values is relatively large. This difference is more noticeable when the CFRC plates are used. The possible reasons for that are discussed in the next section.

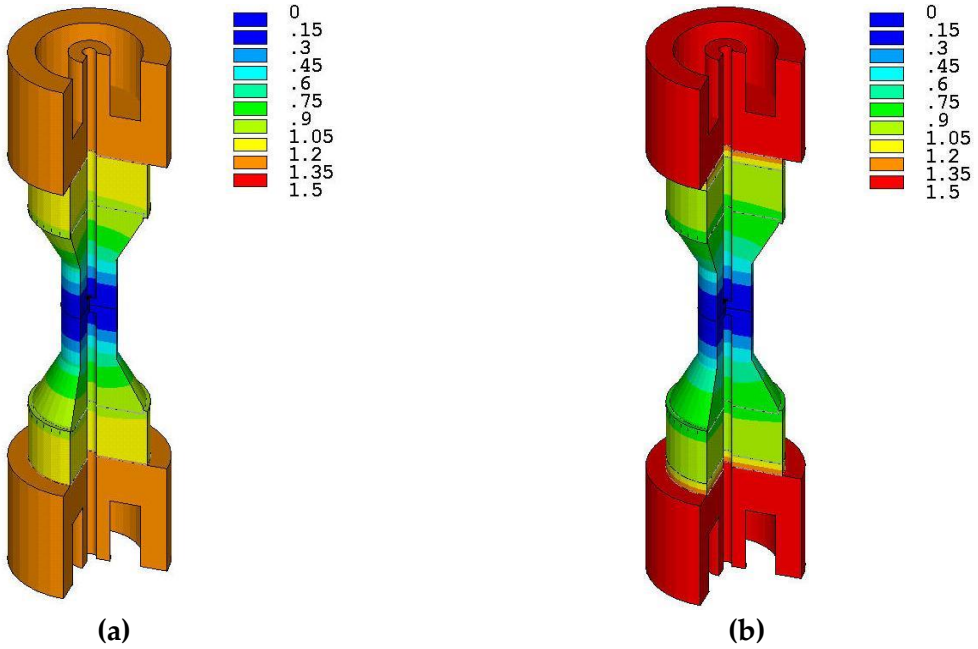

Figure7. FEM-modeled voltage field at 1200 s (holding stage): **(a)** regular setup; **(b)** setup with CFRC spacer**.**

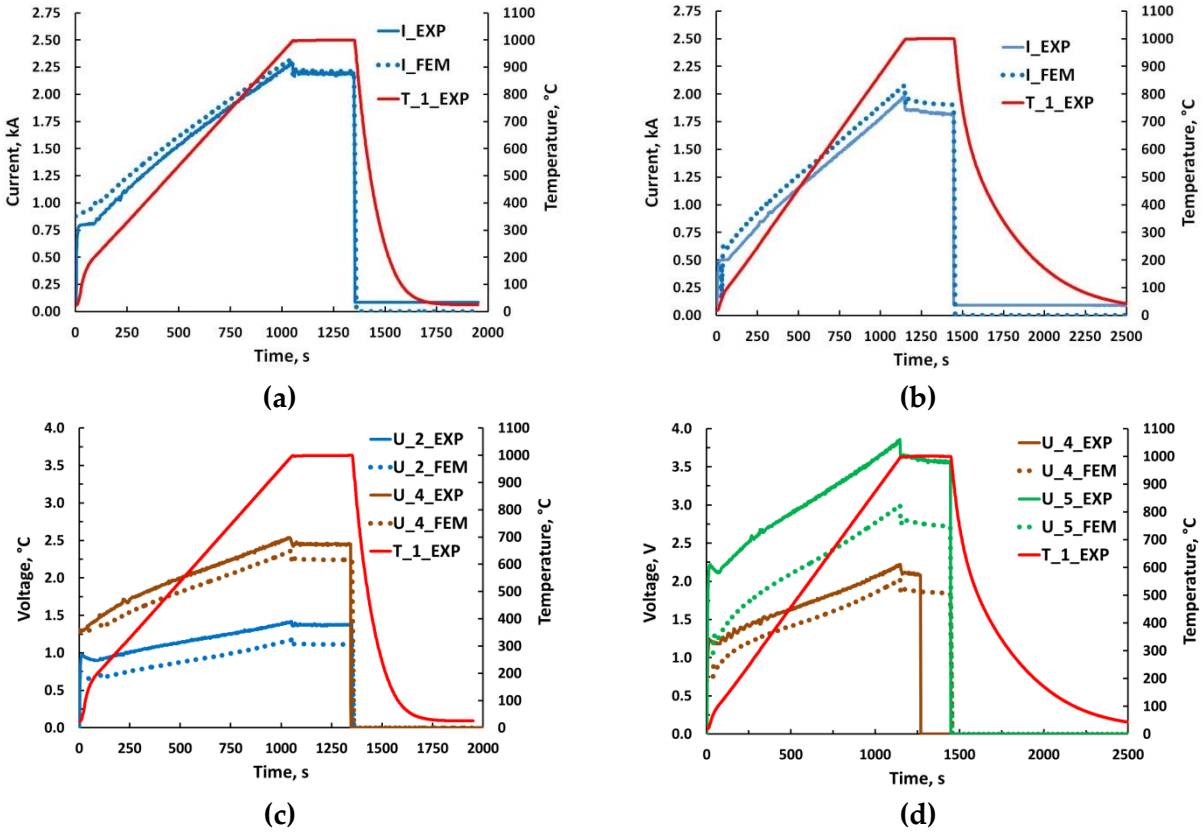

Figure 8. Current **(a-b)** and voltage **(c-d)** development during SPS cycle. Left – regular setup, right – setup with CFRC insert. Solid lines are experimental data and dotted lines are results of FEM modeling. Voltage drop was measured between two symmetric locations in setup.

5. Discussion

From the results discussed above, it follows that the application of CFRC plates has diverse influence on thermal, electrical and energetic parameters during resistive heating in a FAST/SPS device. In particular, the temperature distribution within the setup becomes more homogeneous. The axial temperature gradient decreases, especially near the CFRC insert (Figure 9a). This fact can be important for the sintering of parts with enhanced height, when the axial temperature gradient as an important issue. Furthermore, the application of CFRC plates provides a reduction of power demand and energy consumption. In the discussed case of heating to 1000°C, the energy saving is rather moderate (Figure 9b). However, this can be an important economic and technical advantage, if higher temperatures are used. The application of CFRC plates provides a significant decrease of the temperature of the water-cooled electrodes (Figure 3d). This is a condition for a cost-effective and consistent work of the cooling system. At the same time, the use of CFRC plates leads to a longer cooling time. This increases the total duration of a sintering cycle.

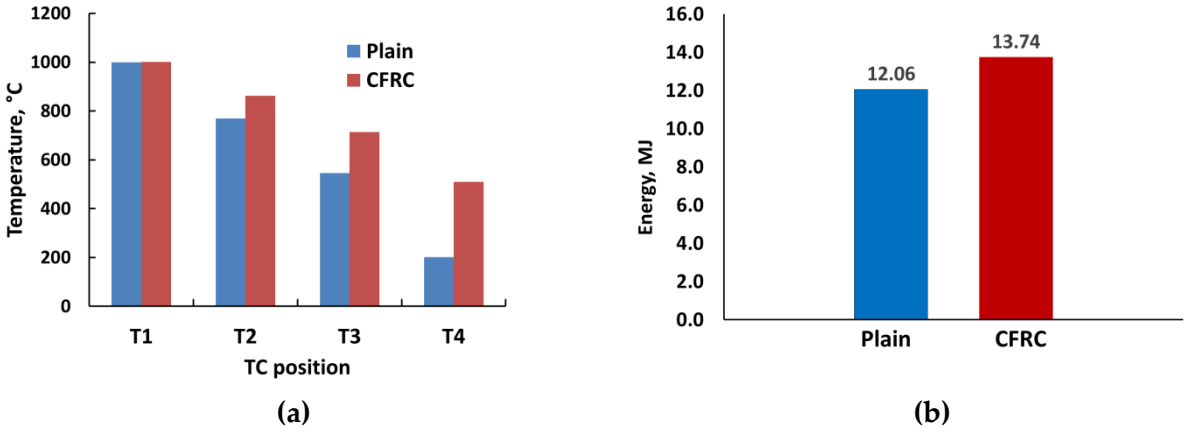

Figure 9. (a) Temperature at 1200 s (dwell segment) measured by thermocouples in different locations and **(b)** total energy consumed with different setups.

The Finite Element Modeling enables an accurate prediction of the temperature distribution within a regular FAST/SPS setup or in a setup with CFRC plates (Figure 8a). Besides, the FEM modeling provides an adequate calculation of the required current (Figure 8c). A slight underestimation of current can be explained by a deviation of real graphite properties from used for modeling. However, the modeled voltage drop between reference points is noticeably lower than observed in experiments (Figures 8c and d). The related resistances calculated by Ohm's law for DC current are shown in Figures 10a and b. The modeled and observed decline of resistance with temperature is a result of the reduction in graphite resistivity with growing temperature. Besides, the calculated resistances are remarkably lower then the measured ones. This discrepancy can be explained by three main reasons or their combination. First, the real resistivity of graphite and CFRC can be higher then applied for modeling. However, this difference is rather small, especially for graphite, because the current modeling was relatively precise. Second, the contact resistances can be underestimated, particularly at low temperature. The resistances of contacts diminish with temperature and applied pressure. Therefore, the discrepancy between calculated and measured resistances becomes lesser with increase in temperature (Figures 10a and b). This argument was used by Sastry et al. [18] and Manière et al. [19]. However, the difference in theoretical and experimental results was also observed between two locations R_2 without any internal contact (Figure 10a). The third possible reason for observed discrepancy is a phase difference between the current and the voltage in the pulsed direct field. In such a case the Ohm's law rearranges to the form $\boldsymbol{U} = \boldsymbol{I}\cdot\boldsymbol{Z}$. Here $\boldsymbol{U}$ = voltage, $\boldsymbol{I}$ = current and $\boldsymbol{Z}$ = impedance. The impedance consists of the real part (resistance) and the imaginary part (reactance). Only the real part of impedance produces the heat. Thus, the voltage is larger

than calculated with the assumption of acting direct current. The reactance appears in electrical circuits with inductors (e.g. coils) and capacitors [20]. Pavia et al. studied the voltage and current pulsing with a SPS machine type 2080 produced by Syntex Inc., Kawasaki, Japan [13]. The authors reported the absence of visual phase difference between voltage and current pulses. However, the resistance within each pulse was not calculated. Furthermore, a non-sinusoidal pulse profile was evident. Apparently, this profile consists of several harmonics. Although all experiments of this work were performed in DC mode (without pulsing), preliminary measurements revealed certain non-sinusoidal AC components. Probably, this leads to RMS (root mean square) averaged voltage measurements, larger than modeled with classical Ohm's law and real DC current. In consequence, the same is true for the calculated resistance values. However, this matter should be studied in more detail.

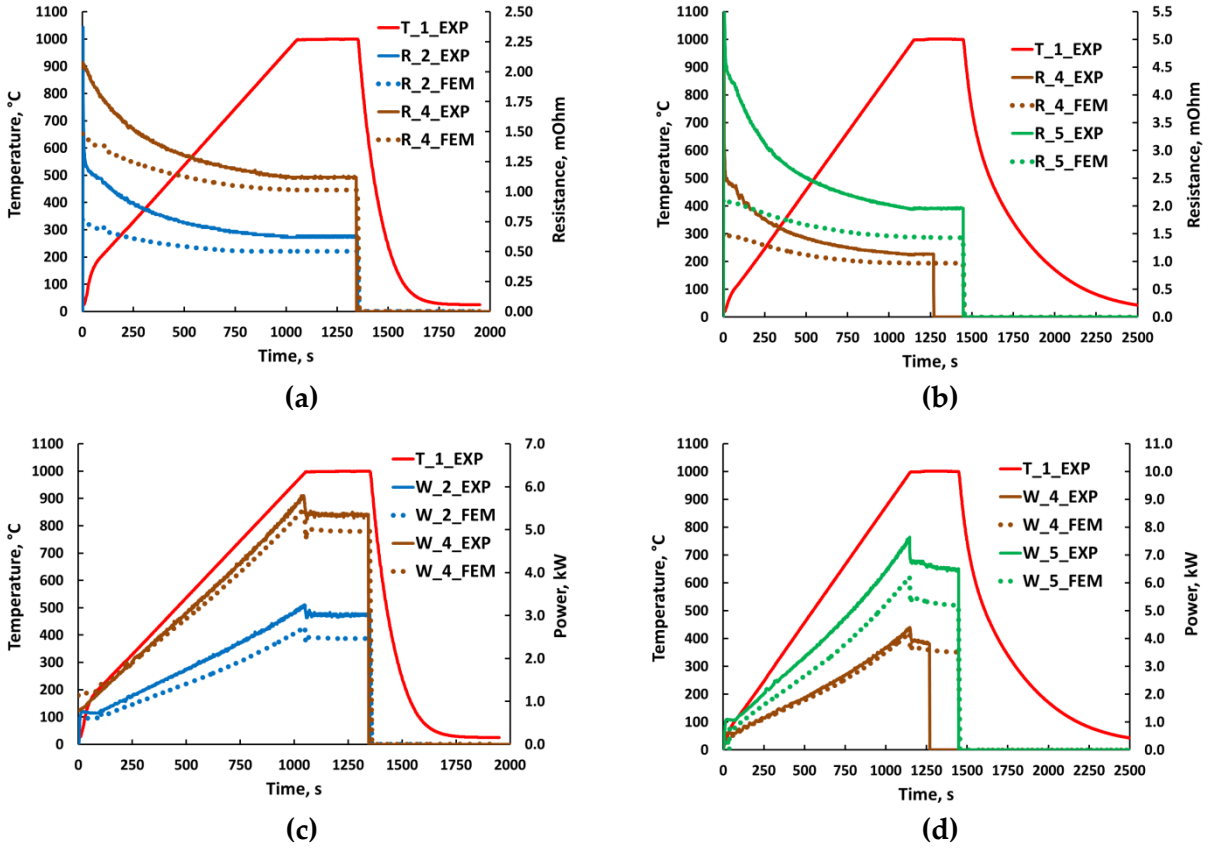

Figure 10. Resistance **(a-b)** and power dissipation **(c-d)** between two symmetrically located probes. Left – regular setup, right – setup with CFRC insert. Solid lines are data calculated from experimental values of voltage and current. Dotted lines are results from FEM modeling.

The development of power dissipation between corresponding locations is presented in Figures 10c and d. As expected from previous analysis, the measured power was in general larger than obtained by FEM modeling. This can be explained by the reasons discussed above for the voltage. If this is the case, the measured power must be considered as an apparent power, while the modeled power is always active power. The ratio between them, called power factor, lies in the range 1 to 1.25 (Figures 10c and d). However, as noted above, this issue requires a special investigation.

6. Conclusions

Insulation of the FAST/SPS setup from the water-cooled electrodes by intermediate CFRC plates results in several important effects. First, the power and the energy needed for heating is remarkably reduced. Second, even more significant, the temperature of electrodes diminishes. Third, the temperature distribution in the setup becomes much more homogeneous, with a particularly pronounced decrease of thermal gradients towards water-cooled electrodes. However, the cooling of the setup with CFRC

insulation needs much more time, comparing to the setup without CFRC insulation. This leads to a prolonged duration of the entire FAST/SPS cycle.

The Finite Element Modeling provides an accurate calculation of the temperature distribution in regular SPS setups, and in setups with CFRC insulation if material properties and boundary conditions are accurately defined. Furthermore, FEM simulation provides adequate results for the electrical current, required for heating. However, the modeled voltage and power are less than the experimental values. This can be a consequence of non-sinusoidal AC components, contained in the heating voltage. This assumption requires an additional investigation.

Author Contributions: Conceptualization, A.M.L. and J.H.; Data curation, A.M.L. and J.H.; Formal analysis, A.M.L. and J.H.; Investigation, A.M.L., J.H. and R.I.; Methodology, J.H. and A.M.L.; Resources, J.H. and R.I.; Supervision, A.M.L. and J.H.; Validation, J.H., and R.I.; Writing—original draft, A.M.L.; Writing—review & editing, A.M.L. and J.H. All authors have read and agreed to the published version of the manuscript.

Funding: This research received no external funding.

Conflicts of Interest: The authors declare no conflict of interest.

References

1. Guillon, O.; Gonzalez-Julian, J.; Dargatz, B.; Kessel, T.; Schierning, G.; Räthel, J.; Herrmann, M. Field-assisted sintering technology/Spark plasma sintering: Mechanisms, materials, and technology developments, *Adv. Eng. Mater.* **2014**, *16*, 830-849.
2. Bram, M.; Laptev, A.M.; Mishra, T.P.; Nur K.; Kindelmann M.; Ihrig M.; Pereira da Silva, J.G.; Steinert, R.; Buchkremer, H.P.; Litnovsky, A.; Klein, F.; Gonzalez-Julian, J.; Guillon, O. Application of electric current-assisted sintering techniques for the processing of advanced materials. *Adv. Eng. Mater.* **2020**, *22*, 2000051.
3. Aleksandrova, E.V.; Ilyina, A.M.; Grigoryev, A.G.; Olevsky, E.A. Contribution of electric current into densification kinetics during spark plasma sintering of conductive powder. *J. Am. Ceram. Soc.* **2015**, *98*, 3509–3517.
4. Vanmeensel, K.; Laptev, A.; Huang, S.G.; Vleugels, J.; Van der Biest, O. The role of the electrical current and field during Pulsed Electric Current Sintering. In *Ceramics and Composites Processing Methods*; Bansal N.P.; Boccaccini, A.R. Eds.; John Wiley & Sons, Inc.: Hoboken, NJ, USA, 2012; pp. 43-74.
5. Mishra, T.P.; Laptev, A.M.; Ziegner, M.; Sistla, S.K.; Kaletsch, A.; Broeckmann, C.; Guillon, O.; Bram, M. Field-assisted sintering/spark plasma sintering of gadolinium-doped ceria with controlled re-oxidation for crack prevention. *Materials* **2020**, *13*, 3184.
6. Dong, P.; Wang, Z.; Wang, W.; Chen, S.; Zhou, J. Understanding the spark plasma sintering from the view of materials joining. *Scr. Mater.* **2016**, *123*, 118–121.
7. Suárez, M.; A. Fernández, A.; Menéndez, J.L.; Torrecillas R.; Kessel, H.U.; Hennicke, J.; Kirchner, R.; Kessel, T. Challenges and opportunities for Spark Plasma Sintering: A key technology for a new generation of materials. In *Sintering Applications*; Ertug, B., Ed.; IntechOpen: London, UK, 2013, pp. 319-342.
8. Tokita, M. Spark Plasma Sintering: Method, systems, applications and industrialization, *Powder Metall. Rev.* **2019**, 8(2), 89-102.
9. Laptev, A.M.; Bram, M.; Vanmeensel, K.; Gonzalez-Julian, J.; Guillon, O. Enhancing efficiency of field assisted sintering by advanced thermal insulation. *J. Mater. Process. Tech.* **2018**, *262*, 326–339.
10. Vanmeensel, K.; Laptev, A.; Hennicke, J.; Vleugels, J.; Van der Biest, O. Modelling of the temperature distribution during field assisted sintering. *Acta Mat.* **2005**, *53*, 4379–4388.
11. McDonald, R.A. Heat content and heat capacity of an extruded graphite from 341° to 1723°K. *J. Chem. Eng. Data* **1965**, *10*, 243.
12. *Carbon fiber-reinforced carbon. Properties, uses, forms supplied.* SGL Carbon Group: Meitingen, Germany, 2004, pp. 1-32.
13. Pavia, A.; Durand, L.; Ajustron, F.; Bley, V.; Chevallier, G.; Peigney, A.; Estournès; C. Electro-thermal measurements and finite element method simulations of a spark plasma sintering device. *J. Mater. Process. Tech.* **2013**, *213*, 1327–1336.
14. Wei, X.; Giuntini, D.; Maximenko, A.L.; Haines, C.H.; Olevsky, E.A. Experimental investigation of electric contact resistance in spark plasma sintering tooling setup. *J. Am. Ceram. Soc.* **2015**, *98*, 3553–3560.

15. Vanmeensel, K.; Laptev, A.; Sheng, H.; Tkachenko, I.; Van der Biest, O.; Vleugels, J. Experimental study and simulation of plastic deformation of zirconia-based ceramics in a pulsed electric current apparatus. *Acta Mat.* **2013**, *61*, 2376–2389.
16. Zavaliangos, A.; Zhang, J.; Krammer, M.; Groza J.R. Temperature evolution during field activated sintering. *Mater. Sci. Eng. A* **2004**, *379*, 218–228.
17. Muñoz, S.; Anselmi-Tamburini, U. Temperature and stress fields evolution during spark plasma sintering processes. *J. Mater. Sci.* **2010**, *45*, 6528–6539.
18. Sastry, K.Y.; Vanmeensel, K.; Froyen L.; Vleugels, J.; Van der Biest, O.; Laptev, A.; Hennicke, J. Simulation of temperature evolution during field assisted sintering of rapidly solidified Al-alloy powder. In Proceedings of the Euro PM 2005: Powder Metallurgy Congress and Exhibition, Prague, Czech Republic, 2-5 October 2005, EPMA: Shrewsbury, UK, 2005; Volume 1, pp. 99-105.
19. Manière, C.; Pavia, A.; Durand, L.; Chevallier, G.; Bley, V.; Afanga, K.; Peigney, A.; Estournès, C. Pulse analysis and electric contact measurements in spark plasma sintering. *Electr. Pow. Syst. Res.* **2015**, *127*, 307-313.
20. Alexander, C.K.; Sadiku, W.N.O. *Fundamentals of Electric Circuit*, 6th ed.; McGraw-Hill, Columbus, OH, USA, 2016; pp. 369-412